The multi-step reconstruction for arbitrarily high order finite volume schemes on the unstructured grids with compact stencils

Yu-Si Zhang*, Yu-Xin Ren*, Qian Wang**
Corresponding author: ryx@tsinghua.edu.cn (Yu-Xin Ren)

* Department of Engineering Mechanics, Tsinghua University, Beijing 100084, China
** Chair of Computational Mathematics and Simulation Science, École Polytechnique Fédérale de Lausanne, 1015 Lausanne, Switzerland

Abstract: In the present paper, a multi-step reconstruction procedure is proposed for the development of high order finite volume schemes on unstructured grids using compact stencil. A recursive algorithm is proposed which can eventually provide sufficient relations for high order reconstruction in a multi-step procedure. Two key elements of this procedure are the partial inversion technique and the continuation technique. The partial inversion can be used not only to obtain lower order reconstruction based on existing reconstruction relations, but also to regularize the existing reconstruction relations to provide new relations for higher order reconstructions. The continuation technique is to extend the regularized relations on the face-neighboring cells to current cell as additional reconstruction relations. This multi-step procedure is operationally compact since in each step only the relations defined on a compact stencil are used. In the present paper, the third and fourth order finite volume schemes based on two-step quadratic and three-step cubic reconstructions are studied.

Keywords: High order schemes, Finite volume method, Unstructured grids

1 Introduction

High order methods have shown great capability in the simulation of flows with multi-scale structures [1]. To handle complicated geometries, various high order numerical methods on the unstructured grids have been developed such as the finite volume (FV) methods [2-9], discontinuous Galerkin (DG) methods [10-14], spectral volume (SV)/spectral difference (SD) methods [15-21], PNPM procedure [22-24] and the hybrid FV/DG methods [25, 26].

Historically, the high order FV methods on the unstructured grids were among the numerical schemes that received earliest attention since they are simpler to construct and apply. The key point of FV schemes is to reconstruct high order representation of the solutions in each cell or control volume. The k-exact FV method was developed by Barth and Frederickson [2]. ENO and WENO schemes were then developed [6, 27-36]. The high order FV schemes usually require a large number of cells in the stencil of the reconstruction procedure. The lack of compactness increases the complexity of the schemes on arbitrary unstructured grids and is also a serious drawback for the parallelization of the code [25, 37]. To overcome this problem, Wang and Ren developed the compact least squares reconstruction (CLSR) scheme [38, 39] on compact stencil. This method is constructed by requiring the variable and its derivatives on the control volume of interest to conserve their averages on the face-neighboring cells. To ensure the non-singularity of the reconstruction procedure, the variational reconstruction (VR) procedure for the high order FV schemes on the unstructured grids was recently proposed [40]. This method can be also applied on a compact stencil and more importantly, can be proved to be non-singular on general shaped unstructured grids. Both CLSR and VR are implicit, and a large system of linear equations should be solved. To design an efficient solution procedure, the CLSR and VR are computed using a certain iterative solution procedure. When solving unsteady flows, they should be coupled with implicit dual time stepping procedure so that only one iteration is performed in each pseudo time step. Using this approach, the FV schemes based on CLSR and VR can be as efficient as those based on the k-exact reconstruction when the implicit time stepping schemes are used. However, when using the explicit time stepping schemes, these methods becomes less efficient because of the implicit nature of these schemes. Therefore, it is desirable to develop an explicit reconstruction algorithm on a compact stencil which can be readily applied in both explicit and implicit time marching schemes.

We notice some approaches with above-mentioned property have been proposed. For example, Yang et al [41] used the Gauss-Green theorem successively to obtain high order distribution of the solution in a control volume. However, it is not able to prove if this approach has the property of k-exactness. Haider et al [42] developed the *Coupled Least Squares* reconstruction by approximating derivatives from higher order to lower order. However, on the unstructured grids, this approach is depended on some claims that are not easy to prove and is very complicated.

In the present paper, the FV scheme based on a multi-step reconstruction (MSR) procedure is proposed. The MSR is a recursive algorithm which can eventually provide sufficient relations for high order reconstruction in a multi-step procedure. Two key elements of this procedure are the partial inversion technique and the continuation technique. The partial inversion can be used not only to obtain lower order reconstruction based on existing reconstruction relations, but also to regularize the existing reconstruction relations to provide new relations for higher order reconstructions. The continuation technique is to extend the regularized relations on the face-neighboring cells to current cell as additional reconstruction relations. During the implementation of this procedure, the cells involved in the reconstruction will increase implicitly. However, this procedure is operationally compact in the sense that in every step of this multi-step procedure, only the information of current and face-neighboring cells is used. As being discussed in [40], this property is sufficient to ease the data transfer between different sub-domains in the parallel computing based on the domain decomposition approach and is also beneficial to reduce the cache missing encountered by traditional high order FV schemes using a very large stencil. The present approach is k-exact. The computational cost is only slightly larger than the traditional k-exact reconstruction using large stencil.

This paper is organized as follows. Section 2 and Section 3 detail the MSR algorithms on 1D and 2D unstructured meshes respectively. In Section 4, numerical results of 1D tests and 2D tests are presented. Finally, conclusions are given in Section 5.

2 High order compact multi-step reconstructions for FV schemes: the 1D case

2.1 Notations

In this section, the 1D MSR is introduced and the spectral property for the corresponding high order FV schemes is analyzed. To facilitate the derivation, some notations are introduced first. In 1D FV methods, the physical domain Ω is decomposed into *N* non-overlapping control volumes (cells). $\Omega_i \equiv \left[x_{i-1/2}, x_{i+1/2}\right]$ is the *i*-th cell and it implies the boundary of Ω is $\partial\Omega = \left\{x_{1/2}, x_{N+1/2}\right\}$. $h_i = x_{i+1/2} - x_{i-1/2}$ is the length of I_i and $x_i = \left(x_{i-1/2} + x_{i+1/2}\right)/2$ is the center of I_i. We denote the *i*-th cell average of variable *u* as

$$\overline{u}_i = \frac{1}{h_i}\int_{\Omega_i} u(x)\,dx\,.$$

In the reconstruction procedure, the variable $u(x)$ is approximated inside each element Ω_i by a local polynomial $u_i(x)$ of the form

$$u_i(x) = \bar{u}_i + \sum_{l=1}^{p} u_i^l \phi_{l,i}(x), \tag{1}$$

where p is the order of the local polynomial, and $\phi_{l,i}(x)$ is the zero-mean basis defined by

$$\phi_{l,i}(x) = (\delta x_i)^l - \frac{1}{h_i}\int_{\Omega_i} (\delta x_i)^l \, dx$$

with $\delta x_i = (x - x_i)/h_i$. The use of the zero-mean basis functions guarantees the cell average of Eq. (1) to be $\bar{u}_i$. Generally speaking, the degree p polynomial reconstruction will result in a p+1 order finite volume scheme. In what follows, the terms 'degree p polynomial reconstruction' and 'p+1-th order reconstruction' are used interchangeably. Specifically, in the next section, the reconstruction of the cubic polynomial using the MSR procedure will be introduced, which can be used to design the 4th order FV schemes.

2.2 1D multi-step reconstruction

In this subsection, the cubic reconstruction is used as an example to introduce the basic idea of the MSR procedure.

In the reconstruction procedure, it is necessary to define the reconstruction stencil which consists of the cells to be used in the reconstruction. Different from the large stencil used in other FV methods (such as k-exact reconstruction or WENO schemes), the compact stencil consists of only face-neighboring cells, on which the MSR is carried out in each recursive step.

In 1D case, for the cubic reconstruction, p=3 in Eq. (1), we define $\boldsymbol{u}_i = \left[u_i^1, u_i^2, u_i^3\right]^T$ as the coefficient vector so that Eq. (1) can be written in the matrix form

$$u_i(x) - \bar{u}_i = \left[\phi_{1,i}, \phi_{2,i}, \phi_{3,i}\right]\boldsymbol{u}_i . \tag{2}$$

In what follows, the MSR is described to determine the unknown coefficient vector $\boldsymbol{u}_i$. Generally speaking, to reconstruct a degree p polynomial, a p-step of reconstruction is needed.

Step 1

Because of the use of the zero-mean basis, Eq. (2) conserve the cell average automatically. On a compact stencil, two additional relations can be derived, in which Eq. (2) is required to conserve the mean on cells Ω_{i-1} and Ω_{i+1}. This will lead to the following *reconstruction relations* (RR, in plural number)

$$\begin{bmatrix} \bar{\phi}_{1,i}^{i-1} & \bar{\phi}_{2,i}^{i-1} & \bar{\phi}_{3,i}^{i-1} \\ \bar{\phi}_{1,i}^{i+1} & \bar{\phi}_{2,i}^{i+1} & \bar{\phi}_{3,i}^{i+1} \end{bmatrix} \boldsymbol{u}_i = \begin{bmatrix} \bar{u}_{i-1} - \bar{u}_i \\ \bar{u}_{i+1} - \bar{u}_i \end{bmatrix}. \tag{3}$$

In Eq. (3), $\overline{(\bullet)}^j$ denotes the averaging operation on cell Ω_j. Eq. (3) can be written in a more compact form as

$$A_i \boldsymbol{u}_i = \boldsymbol{\alpha}_i , \tag{4}$$

where

$$A_i = \begin{bmatrix} \bar{\phi}_{1,i}^{i-1} & \bar{\phi}_{2,i}^{i-1} & \bar{\phi}_{3,i}^{i-1} \\ \bar{\phi}_{1,i}^{i+1} & \bar{\phi}_{2,i}^{i+1} & \bar{\phi}_{3,i}^{i+1} \end{bmatrix}, \; \boldsymbol{\alpha}_i = \begin{bmatrix} \bar{u}_{i-1} - \bar{u}_i \\ \bar{u}_{i+1} - \bar{u}_i \end{bmatrix}.$$

There are 3 unknown coefficients in the vector $\boldsymbol{u}_i$, thus Equation (4) is underdetermined. Therefore, it is not possible to obtain $\boldsymbol{u}_i$ directly. To proceed, here we introduce the so called *partial inversion* *technique* (PIT). Instead of solve all the unknown coefficients at once, the PIT deals with the coefficient related to linear polynomial i.e. u_i^1. Correspondingly, matrix A_i and vector $\boldsymbol{u}_i$ are respectively partitioned into two parts: one related to linear polynomial and the other is the rest. Equation (4) is thus rearranged as

$$\begin{bmatrix} A_{i,1} & A_{i,23} \end{bmatrix} \begin{bmatrix} \boldsymbol{u}_{i,1} \\ \boldsymbol{u}_{i,23} \end{bmatrix} = \boldsymbol{\alpha}_i \tag{5a}$$

or the equivalently

$$A_{i,1}\boldsymbol{u}_{i,1} = \boldsymbol{\alpha}_i - A_{i,23}\boldsymbol{u}_{i,23}, \tag{5b}$$

where

$$A_{i,1} = \begin{bmatrix} \overline{\phi}_{1,i}^{i-1} \\ \overline{\phi}_{1,i}^{i+1} \end{bmatrix},\ A_{i,23} = \begin{bmatrix} \overline{\phi}_{2,i}^{i-1} & \overline{\phi}_{3,i}^{i-1} \\ \overline{\phi}_{2,i}^{i+1} & \overline{\phi}_{3,i}^{i+1} \end{bmatrix},\ \boldsymbol{u}_{i,1} = \begin{bmatrix} u_i^1 \end{bmatrix}^T,\ \boldsymbol{u}_{i,23} = \begin{bmatrix} u_i^2 & u_i^3 \end{bmatrix}^T.$$

Then, $A_{i,1}^+$, the Moore-Penrose inverse of $A_{i,1}$, is firstly computed. One purpose of introducing $A_{i,1}^+$ is to perform linear reconstruction. Indeed, if the contribution of higher order terms corresponding to $A_{i,23}$ is neglected, the use the least-square inversion technique leads to

$$\boldsymbol{u}_{i,1}^{(1)} = A_{i,1}^+\boldsymbol{\alpha}_i, \tag{6}$$

which is the traditional linear k-exact reconstruction. Eq. (6) can be used as the low order reconstruction. However, Eq. (6) is not useful in performing higher order reconstructions. To construct additional constitutive relations for higher order reconstruction, $A_{i,1}^+$ is used again to pre-multiply Eq. (4) or Eq. (5) to obtain the *regularized reconstruction relations* (RRR, in plural number)

$$A_{i,1}^+A_i\boldsymbol{u}_i = A_{i,1}^+\boldsymbol{\alpha}_i \tag{7a}$$

or

$$\begin{bmatrix} A_{i,1}^+A_{i,1} & A_{i,1}^+A_{i,23} \end{bmatrix}\boldsymbol{u}_i = A_{i,1}^+\boldsymbol{\alpha}_i. \tag{7b}$$

We notice that Eq. (7) is the linear mapping of the original reconstruction relation Eq. (3). This property is important which guarantees the k-exactness of the proposed reconstruction procedure. The regulation operation in Eq. (7) is used to reduce the number of the RRR being the number of unknown coefficients of the linear polynomial (or more general, being the number of the lower order polynomial in PIT as shown in Step 2). In summary, the PIT consists of three operations. The first one is to decompose the matrix of RR into lower order and higher order terms. The second one is to compute the Moore-Penrose inverse of the matrix corresponding to the lower order terms, which can be used to obtain the lower order reconstruction when necessary. The third one is to obtain the RRR by the multiplication of the inverse matrix and the RR.

Step 2

The second step is the first recursive step of this MSR scheme. It will be described in detail to demonstrate how higher order reconstruction is obtained from lower order one.

The main idea for achieving higher order reconstruction is to combine the RRR on the current cell (Eq.(7)) and its face-neighboring cells derived in *step 1* to construct new RR. The direct realization of this idea leads to

$$\begin{bmatrix} A_{i,1}^+A_i\boldsymbol{u}_i \\ A_{i-1,1}^+A_{i-1}\boldsymbol{u}_{i-1} \\ A_{i+1,1}^+A_{i+1}\boldsymbol{u}_{i+1} \end{bmatrix} = \begin{bmatrix} A_{i,1}^+\boldsymbol{\alpha}_i \\ A_{i-1,1}^+\boldsymbol{\alpha}_{i-1} \\ A_{i+1,1}^+\boldsymbol{\alpha}_{i+1} \end{bmatrix}. \tag{8}$$

These relations cannot be used directly since $\boldsymbol{u}_i$, $\boldsymbol{u}_{i-1}$ and $\boldsymbol{u}_{i+1}$ are the unknown coefficients on different cells. To solve this problem, the second technique associated with the MSR, namely the *continuation technique* (CT) is proposed. In this technique, when the solution $u(x)$ is smooth, $\boldsymbol{u}_j$ ($j = i-1$ or $i+1$) is expressed as the linear transformation of $\boldsymbol{u}_i$, i.e.

$$\boldsymbol{u}_j = T_{j(\to i)}\boldsymbol{u}_i . \tag{9}$$

In Eq. (9), $T_{j(\to i)}$ (or T_j for short) is a 3×3 square matrix related to grids and basis functions. The derivation of Eq. (9) is given in Appendix A by the continuation of the reconstruction polynomial $u_j(x)$ defined on Ω_j onto Ω_i. Also in Appendix A, we prove that if solution u follows cubic polynomial distribution, Eq. (9) is exact. Substituting Eq. (9) into Eq. (8), we can reach a system of equations only related to $\boldsymbol{u}_i$, i.e.

$$\begin{bmatrix} A_{i,1}^{+}A_i \\ A_{i-1,1}^{+}A_{i-1}T_{i-1} \\ A_{i+1,1}^{+}A_{i+1}T_{i+1} \end{bmatrix}\boldsymbol{u}_i = \begin{bmatrix} A_{i,1}^{+}\boldsymbol{\alpha}_i \\ A_{i-1,1}^{+}\boldsymbol{\alpha}_{i-1} \\ A_{i+1,1}^{+}\boldsymbol{\alpha}_{i+1} \end{bmatrix}, \tag{10a}$$

which can be denoted as

$$B_i\boldsymbol{u}_i = \boldsymbol{\beta}_i . \tag{10b}$$

It is worthwhile to notice that Ω_j is a face-neighboring cell of Ω_i and Eq. (10) is also k-exact.

Eq. (10) is the new RR used in the second step. In this step, the PIT deals with the coefficients related to quadratic polynomial i.e. u_i^1 and u_i^2. We partition matrix B_i and vector $\boldsymbol{u}_i$ into two parts and Eq. (10) represented by partitioned matrices becomes

$$\begin{bmatrix} B_{i,12} & B_{i,3} \end{bmatrix}\begin{bmatrix} \boldsymbol{u}_{i,12} \\ \boldsymbol{u}_{i,3} \end{bmatrix} = \boldsymbol{\beta}_i \tag{11a}$$

or equivalently

$$B_{i,12}\boldsymbol{u}_{i,12} = \boldsymbol{\beta}_i - B_{i,3}\boldsymbol{u}_{i,3}, \tag{11b}$$

where $B_{i,12}$ is the first two columns of B_i, $B_{i,3}$ is the rest of B_i and

$$\boldsymbol{u}_{i,12} = \begin{bmatrix} u_i^1 & u_i^2 \end{bmatrix}^T, \quad \boldsymbol{u}_{i,3} = \begin{bmatrix} u_i^3 \end{bmatrix}.$$

As the PIT in the first step, the Moore-Penrose inverse of $B_{i,12}$ is computed as $B_{i,12}^{+}$. Since there are 3 equations in Equation system (11), it is sufficient to determine a least squares quadratic reconstruction by neglecting the $B_{i,3}\boldsymbol{u}_{i,3}$ term in Eq. (11b), which is given by

$$\boldsymbol{u}_{i,12}^{(2)} = B_{i,12}^{+}\boldsymbol{\beta}_i . \tag{12}$$

To derive higher order reconstruction, the RRR are derived by pre-multiplying Eq. (11) with $B_{i,12}^{+}$, i.e.

$$\begin{gathered} B_{i,12}^{+}B_{i,3}\boldsymbol{u}_i = B_{i,12}^{+}\boldsymbol{\beta}_i \\ \text{or } \begin{bmatrix} B_{i,12}^{+}B_{i,12} & B_{i,12}^{+}B_{i,3} \end{bmatrix}\boldsymbol{u}_i = B_{i,12}^{+}\boldsymbol{\beta}_i \end{gathered} . \tag{13}$$

Step 3

The *step 3* is similar to *step 2* as the 2nd recursive step. The reconstruction relations are provided by the collection of the regularized relations derived in step 2 in Eq. (13) on current cell Ω_i and its face-neighboring cells Ω_j ($j = i-1$ and $i+1$) as

$$\begin{bmatrix} B_{i,12}^{+}B_i\boldsymbol{u}_i \\ B_{i-1,12}^{+}B_{i-1}\boldsymbol{u}_{i-1} \\ B_{i+1,12}^{+}B_{i+1}\boldsymbol{u}_{i+1} \end{bmatrix} = \begin{bmatrix} B_{i,12}^{+}\boldsymbol{\beta}_i \\ B_{i-1,12}^{+}\boldsymbol{\beta}_{i-1} \\ B_{i+1,12}^{+}\boldsymbol{\beta}_{i+1} \end{bmatrix}.$$

The use of CT leads to

$$\begin{bmatrix} B_{i,12}^{+}B_i \\ B_{i-1,12}^{+}B_{i-1}T_{i-1} \\ B_{i+1,12}^{+}B_{i+1}T_{i+1} \end{bmatrix} \boldsymbol{u}_i = \begin{bmatrix} B_{i,12}^{+}\boldsymbol{\beta}_i \\ B_{i-1,12}^{+}\boldsymbol{\beta}_{i-1} \\ B_{i+1,12}^{+}\boldsymbol{\beta}_{i+1} \end{bmatrix}, \tag{14a}$$

which can be denoted as

$$C_i \boldsymbol{u}_i = \boldsymbol{\gamma}_i . \tag{14b}$$

There are 6 relations in Eq. (14). It is sufficient to give the least square cubic reconstruction by

$$\boldsymbol{u}_i = C_i^{+}\boldsymbol{\gamma}_i ,$$

where C_i^{+} is the Moore-Penrose inverse of C_i. Since we use the cubic reconstruction to demonstrate the MSR procedure, the PIT is not needed in the last step.

Remark 1. It can be proved that all RR and RRR presented in step 1-3 are exactly satisfied when solution $u(x)$ follows cubic polynomial distribution. Therefore, the present reconstruction is k-exact. The k-exactness of the present procedure ensures that the spatially 4th order accuracy can be achieved theoretically for the FV schemes using the cubic reconstructions.

Remark 2. The RRR can be weighted to change relative importance of different relations. For example, Eqs. (10a) and (14a) can be changed respectively to

$$\begin{bmatrix} A_{i,1}^{+}A_i \\ \omega A_{i-1,1}^{+}A_{i-1}T_{i-1} \\ \omega A_{i+1,1}^{+}A_{i+1}T_{i+1} \end{bmatrix} \boldsymbol{u}_i = \begin{bmatrix} A_{i,1}^{+}\boldsymbol{\alpha}_i \\ \omega A_{i-1,1}^{+}\boldsymbol{\alpha}_{i-1} \\ \omega A_{i+1,1}^{+}\boldsymbol{\alpha}_{i+1} \end{bmatrix} \tag{15}$$

and

$$\begin{bmatrix} B_{i,12}^{+}B_i \\ \omega B_{i-1,12}^{+}B_{i-1}T_{i-1} \\ \omega B_{i+1,12}^{+}B_{i+1}T_{i+1} \end{bmatrix} \boldsymbol{u}_i = \begin{bmatrix} B_{i,12}^{+}\boldsymbol{\beta}_i \\ \omega B_{i-1,12}^{+}\boldsymbol{\beta}_{i-1} \\ \omega B_{i+1,12}^{+}\boldsymbol{\beta}_{i+1} \end{bmatrix}. \tag{16}$$

The weight is chosen as $\omega \in (0,1]$ since the RRR of the central cell should be more important than those of the neighboring cells. It is trivial to show that the introduction of the weights does not affect the k-exactness of the reconstruction procedure. The impact of the weights will be discussed in Section 2.3.

Remark 3. *Steps 1-3* only demonstrate a 4th order cubic reconstruction procedure with MSR. The recursive *steps 2* and *3* are used to raise order of reconstruction by 1, respectively. When a 5th order reconstruction is required, we use quartic polynomial i.e. *p*=4 in Equation (1) and the corresponding vector $\boldsymbol{u}_i = \left[u_i^1, u_i^2, u_i^3, u_i^4\right]^T$ is to be determined. In this case, the reconstructions with 4 stages can be used, in which the first and the second stages are basically the same as the cubic reconstruction, the third stage is added to construct the RRR for quartic reconstruction, and the last (fourth) stage is similar to the third stage of the cubic reconstruction. It is then clear that arbitrary order reconstruction can be easily achieved by repeating the recursive steps. In general, the reconstruction for *n*-th order FV schemes requires n-1 steps with *Step 2-Step n-1* implemented recursively.

2.3 Fourier analysis

In this section, Fourier analysis of the semi-discretized FV scheme using the MSR is presented for the discussion of dispersion, dissipation and stability properties of the proposed scheme. The governing equation is a scalar linear wave equation

$$\frac{\partial u}{\partial t} + \frac{\partial f}{\partial x} = 0 , \tag{17}$$

where $f = au$ and a is a positive constant. For simplicity, we assume that the grids are uniform i.e. $h_i \equiv h$. The integral form of Eq. (17) on cell Ω_i is

$$\frac{\partial \bar{u}_i}{\partial t} = -\frac{1}{h}\left(f_{i+1/2} - f_{i-1/2} \right), \tag{18}$$

where $f_{i+1/2}$ is exact flux. The semi-discrete scheme of Eq. (18) is

$$\frac{\partial \bar{u}_i}{\partial t} = -\frac{1}{h}\left(\hat{f}_{i+1/2} - \hat{f}_{i-1/2} \right), \tag{19}$$

where $\hat{f}_{i+1/2}$ is numerical flux. In the analysis, upwind fluxes are used such that

$$\hat{f}_{i+1/2} = a u^L_{i+1/2}, \tag{20}$$

where $u^L_{i+1/2}$ denotes approximation of $u(x)$ at $x_{i+1/2}$ computed using the MSR on the left-side cell Ω_i.

Fourier analysis is presented to study the spectral behavior of 4th order FV scheme using cubic MSR. A single wave $u(x,t) = A_m(t) e^{ik_m x}$ with a wavenumber k_m is considered as the solution in the analysis, leading to the cell average

$$\bar{u}_i = \frac{A_m}{ik_m h}\left(e^{ik_m x_{i+1/2}} - e^{ik_m x_{i-1/2}} \right) \tag{21}$$

and exact flux

$$f_{i+1/2} = a A_m e^{ik_m x_{i+1/2}}$$

respectively. These formulations are then introduced to the integral form of Eq. (18) which gives

$$\frac{\partial A_m}{\partial t} + ik_m a A_m = 0 .$$

Correspondingly, using Eq. (21) in the MSR, the semi-discrete scheme Eq. (19) with the numerical flux Eq. (20) becomes

$$\frac{\partial A_m}{\partial t} + ik'_m a A_m = 0 ,$$

where

$$\frac{k'_m}{k_m} = \frac{\hat{f}_{i+1/2} - \hat{f}_{i-1/2}}{f_{i+1/2} - f_{i-1/2}} .$$

The wavenumber k_m and k'_m can be scaled as

$$\kappa = k_m h, \ \ \kappa' = k'_m h ,$$

where κ is called scaled wavenumber and κ' is called modified wavenumber. The relation of these two wavenumbers can be written as

$$\kappa' = \frac{\hat{f}_{i+1/2} - \hat{f}_{i-1/2}}{f_{i+1/2} - f_{i-1/2}} \kappa .$$

In the finite volume schemes, κ' is in general complex whose real part is associated with the dispersive error and imaginary part is associated with the dissipative error. It can be calculated as a function of the scaled wavenumber κ. The specific forms of κ' for 2nd to 4th order reconstructions are given below.

The 2nd order MSR:

$$\mathrm{Re}(\kappa') = \frac{3}{2}\sin(\kappa) - \frac{1}{4}\sin(2\kappa) ,$$

$$\mathrm{Im}(\kappa') = -\frac{3}{4} + \cos(\kappa) - \frac{1}{4}\cos(2\kappa).$$

The 3rd order MSR:

$$\mathrm{Re}(\kappa') = \frac{(69+78\omega^2)\sin(\kappa) + (-12+24\omega^2)\sin(2\kappa) + (1-10\omega^2)\sin(3\kappa)}{48(1+2\omega^2)},$$

$$\mathrm{Im}(\kappa') = \frac{-34-92\omega^2 + (47+106\omega^2)\cos(\kappa) + (-14-4\omega^2)\cos(2\kappa) + (1-10\omega^2)\cos(3\kappa)}{48(1+2\omega^2)}.$$

The 4th order MSR:

$$\mathrm{Re}(\kappa') = \frac{1}{q_0}\left(q_1\sin(\kappa) + q_2\sin(2\kappa) + q_3\sin(3\kappa) + q_4\sin(4\kappa)\right),$$

$$\mathrm{Im}(\kappa') = \frac{1}{q_0}\left(q_5 + q_6\cos(\kappa) + q_7\cos(2\kappa) + q_8\cos(3\kappa) + q_9\cos(4\kappa)\right),$$

where

$$\begin{cases} q_0 = 192(1+\omega^2)(1+2\omega^2)^2 \\ q_1 = 302 + 1296\omega^2 + 1648\omega^4 + 1200\omega^6 \\ q_2 = -66 - 100\omega^2 + 288\omega^4 - 224\omega^6 \\ q_3 = 6 - 80\omega^2 - 336\omega^4 - 16\omega^6 \\ q_4 = 1 + 26\omega^2 + 80\omega^4 + 16\omega^6 \\ q_5 = -125 - 730\omega^2 - 1360\omega^4 - 560\omega^6 \\ q_6 = 184 + 1004\omega^2 + 1760\omega^4 + 784\omega^6 \\ q_7 = -68 - 256\omega^2 - 256\omega^4 - 224\omega^6 \\ q_8 = 8 - 44\omega^2 - 224\omega^4 - 16\omega^6 \\ q_9 = 1 + 26\omega^2 + 80\omega^4 + 16\omega^6 \end{cases}.$$

There is a parameter ω that is the weight introduced in Eqs. (15) and (16). In the present paper, we usually choose $\omega = 1$. A smaller value of ω can be adopted to emphasize the contribution of the central cell. An optimization procedure of ω is implemented by minimizing cost function [38, 43]

$$E = \frac{1}{e^{\nu\pi}}\int_0^\pi e^{\nu(\pi-\kappa)}\left(\mathrm{Re}(\kappa') - \kappa\right)^2 d\kappa. \tag{22}$$

We choose $\nu = 4$ in Equation (22) for 3rd and 4th order schemes and find that the cost function is monotonically increasing with ω in $(0,1]$. It indicates that the smaller the weight ω, the smaller the dispersion error. On the other hand, a very small ω tends to make the reconstruction singular. In the present paper, $\omega = 0.2$ is chosen as an optimized case since the dispersion relation changes very little when ω is smaller than 0.2.

In Fig. 1a, the real parts of κ' are plotted for the 2nd, 3rd and 4th order MSRs. The 4th order central difference scheme(C4) [44] is also presented for comparison. It is evident that higher order schemes produce smaller dispersion errors. Compared to the standard 4th order central difference scheme, FV schemes based on the cubic MSR stay closer to the exact dispersion relations over a wider range of wavenumber. The optimized 4th order reconstruction with $\omega = 0.2$ is better than the standard case with $\omega = 1$. In Fig. 1b, the imaginary parts of κ' are plotted for the 2nd, 3rd, 4th order multi-step schemes and the C4 scheme to compare the dissipation properties of different schemes. It can be noted that the increase of the accuracy reduces dissipative errors in the low wavenumber range, but slightly affects intermediate wavenumber range. The measure of phase error $\mathrm{Re}(\kappa')/\kappa - 1$ is more intuitive to show the phase speed. In Fig. 2, this information for different schemes is also presented. The improved of dispersion property for the optimized multi-step scheme is clearly shown.

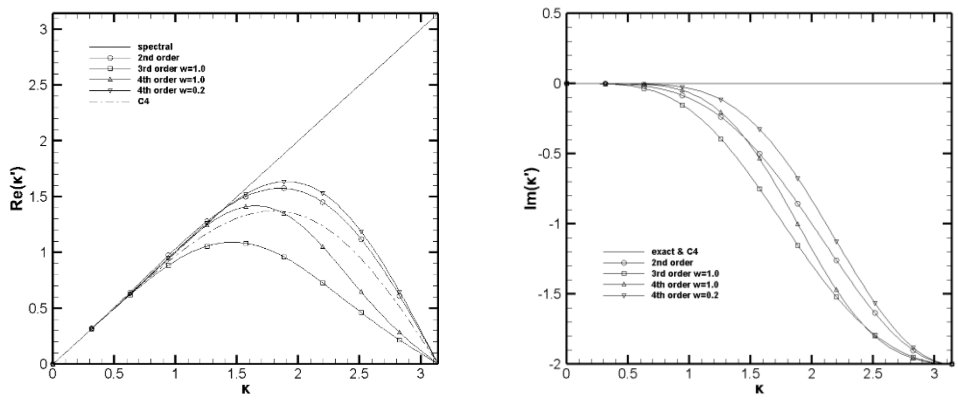

(a) (b)

Fig. 1: Dispersion and dissipation properties of the 2nd to 4th order multi-step schemes.

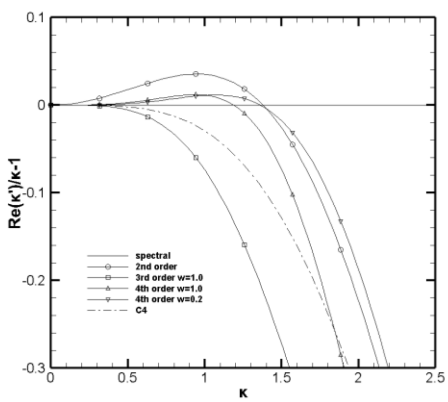

Fig. 2: Dispersion errors of the 2nd to 4th order multi-step schemes.

3 High order compact FV schemes based on the multi-step reconstruction for the 2D case

3.1 Notations

In 2D case, we are interested in the FV method on the unstructured triangular grids. The computational domain Ω is composed of a collection of *N* non-overlapping space filling triangles, i.e.

$$\Omega = \bigcup_{i=1}^{N} \Omega_i ,$$

where Ω_i is the *i*-th cell. For a specific triangular cell Ω_i, the boundary is composed of 3 sides or interfaces

$$\partial\Omega_i = \bigcup_{m=1}^{3} I_m .$$

Supposing 3 nodes (vertices) of the specific cell Ω_i is point 1, 2 ,3 and coordinates of those points are $(X_1, Y_1), (X_2, Y_2), (X_3, Y_3)$ respectively (capital letters are used here to be distinguished from coordinates of cell centers). The volume of Ω_i is computed using

$$\left|\Omega_i\right| = \frac{1}{2}\left[\left(X_1 - X_2\right)\left(Y_1 + Y_2\right) + \left(X_2 - X_3\right)\left(Y_2 + Y_3\right) + \left(X_3 - X_1\right)\left(Y_3 + Y_1\right)\right].$$

The nodes have to be numbered in the anti-clockwise direction to obtain a positive volume. The center of Ω_i is defined as

$$\left(x_i, y_i\right) = \left(\frac{X_1 + X_2 + X_3}{3}, \frac{Y_1 + Y_2 + Y_3}{3}\right).$$

We denote the i-th cell average of variable $u\left(x\right)$ as

$$\overline{u}_i = \frac{1}{\left|\Omega_i\right|}\int_{\Omega_i} u d\Omega. \tag{23}$$

In the reconstruction procedure, the variable $u\left(x\right)$ is approximated inside each element Ω_i by a local polynomial $u_i\left(x\right)$ of the form:

$$u_i\left(\boldsymbol{x}\right) = \overline{u}_i + \sum_{l=1}^{NOC(p)} u_i^l \phi_{l,i}\left(\boldsymbol{x}\right), \tag{24}$$

where $NOC\left(p\right)$ is the number of unknown coefficients for degree p polynomial e.g. $NOC\left(1\right) = 2, NOC\left(2\right) = 5, NOC\left(3\right) = 9$. In this paper, we take basis function $\phi_{l,i}$ be the zero-mean basis that is

$$\phi_{l,i}\left(\boldsymbol{x}\right) = \delta x_i^m \delta y_i^n - \overline{\delta x_i^m \delta y_i^n},$$

where $\delta x_i = \left(x - x_i\right)/h_i, \delta y_i = \left(y - y_i\right)/h_i$, $\overline{\delta x_i^m \delta y_i^n} = \frac{1}{\left|\Omega_i\right|}\int_{\Omega_i} \delta x_i^m \delta y_i^n d\Omega$, and m, n are powers of corresponding l-th basis function. The length scale h_i for each triangular cell is given by

$$h_i = \max\left(r_i, \sqrt{\left|\Omega_i\right|}\right),$$

where r_i denotes the radius of the circumcircle of cell Ω_i. The 4th-order reconstruction will be presented in Section 3.2 to obtain coefficients of the following cubic polynomial

$$\begin{aligned} u_i\left(\boldsymbol{x}\right) = \overline{u}_i &+ u_i^1\left(\delta x_i - \overline{\delta x_i}\right) + u_i^2\left(\delta y_i - \overline{\delta y_i}\right) + u_i^3\left(\delta x_i^2 - \overline{\delta x_i^2}\right) \\ &+ u_i^4\left(\delta x_i \delta y_i - \overline{\delta x_i \delta y_i}\right) + u_i^5\left(\delta y_i^2 - \overline{\delta y_i^2}\right) + u_i^6\left(\delta x_i^3 - \overline{\delta x_i^3}\right) \\ &+ u_i^7\left(\delta x_i^2 \delta y_i - \overline{\delta x_i^2 \delta y_i}\right) + u_i^8\left(\delta x_i \delta y_i^2 - \overline{\delta x_i \delta y_i^2}\right) + u_i^9\left(\delta y_i^3 - \overline{\delta y_i^3}\right) \end{aligned}. \tag{25}$$

In Section 3.3, we will present high order FV scheme solving 2D Euler equations.

3.2 2-D multi-step reconstruction

The reconstruction procedure on 2D grids is essentially same as that in Section 1. In this section, a 4th-order MSR is presented as Section 1. The boundary treatment and the selection of weights are also studied to demonstrate the differences from 1D case.

For a 4th order reconstruction, $p = 3$ and $NOC\left(p\right) = 9$ in Eq. (24). The specific form of cubic polynomial in element Ω_i has been presented in Eq. (25). We define the coefficient vector $\boldsymbol{u}_i = \begin{bmatrix} u_i^1 & u_i^2 & u_i^3 & u_i^4 & u_i^5 & u_i^6 & u_i^7 & u_i^8 & u_i^9 \end{bmatrix}^T$, which leads Eq. (24) into the matrix form

$$u_i\left(x\right) - \overline{u}_i = \begin{bmatrix} \phi_{1,i} & \phi_{2,i} & \phi_{3,i} & \phi_{4,i} & \phi_{5,i} & \phi_{6,i} & \phi_{7,i} & \phi_{8,i} & \phi_{9,i} \end{bmatrix} \boldsymbol{u}_i. \tag{26}$$

As the reconstruction procedure has been introduced in detail in Section 2. It is only briefly introduced here.

Step 1

For a triangular cell Ω_i, it has 3 cells $\Omega_{j_1}, \Omega_{j_2}, \Omega_{j_3}$ as its direct neighbors. We denote $\overline{(\bullet)}^j$ as the average on the cell Ω_j. The averages of Eq. (26) on $\Omega_{j_1}, \Omega_{j_2}, \Omega_{j_3}$ give

$$\begin{bmatrix} \overline{\phi_{1,i}}^{j_1} & \overline{\phi_{2,i}}^{j_1} & \cdots & \overline{\phi_{9,i}}^{j_1} \\ \overline{\phi_{1,i}}^{j_2} & \overline{\phi_{2,i}}^{j_2} & \cdots & \overline{\phi_{9,i}}^{j_2} \\ \overline{\phi_{1,i}}^{j_3} & \overline{\phi_{2,i}}^{j_3} & \cdots & \overline{\phi_{9,i}}^{j_3} \end{bmatrix} \boldsymbol{u}_i = \begin{bmatrix} \overline{u}_i^{j_1} - \overline{u}_i \\ \overline{u}_i^{j_2} - \overline{u}_i \\ \overline{u}_i^{j_3} - \overline{u}_i \end{bmatrix}.$$

The reconstruction procedure requires $u_i(\boldsymbol{x})$ to conserve the cell averages on its face neighboring cells, i.e. $\overline{u}_i^j = \overline{u}_j$, which leads to the following primary RR

$$\begin{bmatrix} \overline{\phi_{1,i}}^{j_1} & \overline{\phi_{2,i}}^{j_1} & \cdots & \overline{\phi_{9,i}}^{j_1} \\ \overline{\phi_{1,i}}^{j_2} & \overline{\phi_{2,i}}^{j_2} & \cdots & \overline{\phi_{9,i}}^{j_2} \\ \overline{\phi_{1,i}}^{j_3} & \overline{\phi_{2,i}}^{j_3} & \cdots & \overline{\phi_{9,i}}^{j_3} \end{bmatrix} \boldsymbol{u}_i = \begin{bmatrix} \overline{u}_{j_1} - \overline{u}_i \\ \overline{u}_{j_2} - \overline{u}_i \\ \overline{u}_{j_3} - \overline{u}_i \end{bmatrix},$$

or in more compact form

$$A_i \boldsymbol{u}_i = \boldsymbol{\alpha}_i. \tag{27}$$

There are 9 unknown coefficients in the vector $\boldsymbol{u}_i$, thus the 3-equation system Equation (27) is underdetermined. By using the PIT, Eq. (27) is partitioned as

$$\begin{bmatrix} A_{i,1} & A_{i,23} \end{bmatrix} \begin{bmatrix} \boldsymbol{u}_{i,1} \\ \boldsymbol{u}_{i,23} \end{bmatrix} = \boldsymbol{\alpha}_i \tag{28a}$$

or equivalently

$$A_{i,1}\boldsymbol{u}_{i,1} = \boldsymbol{\alpha}_i - A_{i,23}\boldsymbol{u}_{i,23}, \tag{28b}$$

where

$$A_{i,1} = \begin{bmatrix} \overline{\phi_{1,i}}^{j_1} & \overline{\phi_{2,i}}^{j_1} \\ \overline{\phi_{1,i}}^{j_2} & \overline{\phi_{2,i}}^{j_2} \\ \overline{\phi_{1,i}}^{j_3} & \overline{\phi_{2,i}}^{j_3} \end{bmatrix}, \quad A_{i,23} = \begin{bmatrix} \overline{\phi_{3,i}}^{j_1} & \cdots & \overline{\phi_{9,i}}^{j_1} \\ \overline{\phi_{3,i}}^{j_2} & \cdots & \overline{\phi_{9,i}}^{j_2} \\ \overline{\phi_{3,i}}^{j_3} & \cdots & \overline{\phi_{9,i}}^{j_3} \end{bmatrix}$$

$$\boldsymbol{u}_{i,1} = \begin{bmatrix} u_i^1 & u_i^2 \end{bmatrix}^T, \quad \boldsymbol{u}_{i,23} = \begin{bmatrix} u_i^3 & \cdots & u_i^9 \end{bmatrix}^T. \tag{28c}$$

In Eq. (28), the components of $\boldsymbol{u}_{i,1}$ are the linear terms, and the components of $\boldsymbol{u}_{i,23}$ are higher order terms. The least-square solution leads to the coefficient vector for linear polynomial

$$\boldsymbol{u}_{i,1}^{(1)} = A_{i,1}^{+}\boldsymbol{\alpha}_i - A_{i,1}^{+}A_{i,23}\boldsymbol{u}_{i,23}, \tag{29}$$

where $A_{i,1}^{+}$ represents the Moore-Penrose inverse of $A_{i,1}$. The corresponding RRR are

$$A_{i,1}^{+}A_i\boldsymbol{u}_i = A_{i,1}^{+}\boldsymbol{\alpha}_i. \tag{29}$$

Step 2

We use CT to express the vector of the unknown coefficients $\boldsymbol{u}_j$ on Ω_j in terms of that on Ω_i, i.e.

$$\boldsymbol{u}_j = T_{j(\to i)}\boldsymbol{u}_i\,, \tag{30}$$

where Ω_j is one of $\Omega_{j_1}, \Omega_{j_2}, \Omega_{j_3}$, the face neighboring cell of Ω_i, and $T_{j(\to i)}$ (T_j for short) is a 9×9 transformation matrix whose detailed form is presented in Appendix A. Applying Eq. (30) to the RRR defined on Ω_j, we obtain the RR of Step 2

$$\begin{bmatrix} A_{i,1}^{+}A_i \\ A_{j_1,1}^{+}A_{j_1}T_{j_1} \\ A_{j_2,1}^{+}A_{j_2}T_{j_2} \\ A_{j_3,1}^{+}A_{j_3}T_{j_3} \end{bmatrix}\boldsymbol{u}_i = \begin{bmatrix} A_{i,1}^{+}\boldsymbol{\alpha}_i \\ A_{j_1,1}^{+}\boldsymbol{\alpha}_{j_1} \\ A_{j_2,1}^{+}\boldsymbol{\alpha}_{j_2} \\ A_{j_3,1}^{+}\boldsymbol{\alpha}_{j_3} \end{bmatrix}, \tag{31a}$$

which can be denoted as

$$B_i\boldsymbol{u}_i = \boldsymbol{\beta}_i\,. \tag{31b}$$

Applying the PIT to Eq. (31b), we partition matrix B_i and vector $\boldsymbol{u}_i$ into two parts as

$$\begin{bmatrix} B_{i,12} & B_{i,3} \end{bmatrix}\begin{bmatrix} \boldsymbol{u}_{i,12} \\ \boldsymbol{u}_{i,3} \end{bmatrix} = \boldsymbol{\beta}_i$$

or equivalently

$$B_{i,12}\boldsymbol{u}_{i,12} = \boldsymbol{\beta}_i - B_{i,3}\boldsymbol{u}_{i,3}\,,$$

where $B_{i,12}$ is the first 5 columns of B_i corresponding to the linear and quadratic terms, $B_{i,3}$ is the rest of B_i and

$$\boldsymbol{u}_{i,12} = \begin{bmatrix} u_i^1 & \dots & u_i^5 \end{bmatrix}^T,\ u_{i,3} = \begin{bmatrix} u_i^6 & \dots & u_i^9 \end{bmatrix}^T.$$

There are generally $2\times 4 = 8$ equations in Eq. (31) for triangular grids while the number of unknown coefficients of quadratic polynomial is 5. This means the least-square solution to determine $\boldsymbol{u}_{i,12}$ is applicable, which is

$$\boldsymbol{u}_{i,12}^{(2)} = B_{i,12}^{+}\boldsymbol{\beta}_i - B_{i,12}^{+}B_{i,3}\boldsymbol{u}_{i,3}\,. \tag{32}$$

The multiplication of $B_{i,12}^{+}$ with Eq. (31b) results in the RRR of Step 2

$$B_{i,12}^{+}B_{i,3}\boldsymbol{u}_i = B_{i,12}^{+}\boldsymbol{\beta}_i\,.$$

Step 3

The combination of the RRR on current and face-neighboring cells and the application of CT result in the RR of Step 3

$$\begin{bmatrix} B_{i,12}^{+}B_i \\ B_{j_1,12}^{+}B_{j_1}T_{j_1} \\ B_{j_2,12}^{+}B_{j_2}T_{j_2} \\ B_{j_3,12}^{+}B_{j_3}T_{j_3} \end{bmatrix}\boldsymbol{u}_i = \begin{bmatrix} B_{i,12}^{+}\boldsymbol{\beta}_i \\ B_{j_1,12}^{+}\boldsymbol{\beta}_{j_1} \\ B_{j_2,12}^{+}\boldsymbol{\beta}_{j_2} \\ B_{j_3,12}^{+}\boldsymbol{\beta}_{j_3} \end{bmatrix}, \tag{33a}$$

which can be denoted as

$$C_i\boldsymbol{u}_i = \boldsymbol{\gamma}_i\,. \tag{33b}$$

For triangular grids, there are $5\times 4 = 20$ equations in Eq. (33) and it is sufficient to solve the vector of unknown coefficients of the cubic reconstruction polynomial using the least-squares technique, i.e.

$$\boldsymbol{u}_i = C_i^{+}\boldsymbol{\gamma}_i\,,$$

where C_i^{+} is the Moore-Penrose inverse of C_i ..

Remark 4. Generally speaking, for the cubic reconstruction, the least-squares solutions of the linear and quadratic reconstructions Eqs. (6, 12, 29, 32) for both 1D and 2D cases need not to be solved. However, if the *p*-adaptation procedure is adopted, these equations provide efficient methods to compute the lower order reconstructions. The use of the *p*-adaptation technique together with the MSR will be discussed in a future paper.

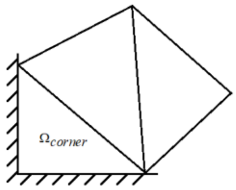

Fig. 3: Diagram of a corner cell Ω_{corner}.

Remark 5. Boundary treatment. In the MSR, the technique of least-squares is used in every step. Therefore, it is necessary to ensure sufficient number of RR on the boundary cells with at least one edge on the boundaries of the domain. It can be found in Fig. 3 that some cells e.g. corner cell Ω_{corner} may not satisfy this requirement. For this reason, some special treatment is needed for the boundary cells. We denote that Ω_i is a boundary cell usually with two neighboring control volumes Ω_{j_k} $(k=1,2)$ as internal cells. For some special case e.g. Fig. 3, there is only one internal neighboring cell. In such case, the only internal RR will be presented in equations. To ensure there are always sufficient number of relations in the reconstruction algorithms, an asynchronous procedure is proposed. The idea of this procedure is in each step to perform the MSR for the internal cells first, then to use the resulting RRR on cells that are adjacent to the boundary cell (after applying the CT) as the RR of the boundary cell of the same step. In Step 1, the proposed procedure is firstly applied on the internal cells to obtain the RRR Eq. (29). Then on boundary cell Ω_i, Eq. (29) of the face-neighboring internal cells Ω_{j_k} $(k=1,2)$ is used as the RR of cell Ω_i, i.e.

$$\begin{bmatrix} A^+_{j_1,1}A_{j_1}T_{j_1} \\ A^+_{j_2,1}A_{j_2}T_{j_2} \end{bmatrix} \boldsymbol{u}_i = \begin{bmatrix} A^+_{j_1,1}\boldsymbol{\alpha}_{j_1} \\ A^+_{j_2,1}\boldsymbol{\alpha}_{j_2} \end{bmatrix},$$

which can be denoted as

$$A_i\boldsymbol{u}_i = \boldsymbol{\alpha}_i,$$

where A_i is a system with $2\times 2=4$ equations when the boundary cell has two neighboring internal cells (2 equations for case with only one neighboring internal cell). Therefore, it is sufficient to obtain the RRR of the first step. In *Step 2*, the same procedure is used. At first, we implement *Step 2* on internal cells. Then *Step 2* is implemented on boundary cell Ω_i using the following RR

$$\begin{bmatrix} A^+_{i,1}A_i \\ B^+_{j_1,12}B_{j_1}T_{j_1} \\ B^+_{j_2,12}B_{j_2}T_{j_2} \end{bmatrix} \boldsymbol{u}_i = \begin{bmatrix} A^+_{i,1}\boldsymbol{\alpha}_i \\ B^+_{j_1,12}\boldsymbol{\beta}_{j_1} \\ B^+_{j_2,12}\boldsymbol{\beta}_{j_2} \end{bmatrix}, \tag{34a}$$

which can be denoted as

$$B_i\boldsymbol{u}_i = \boldsymbol{\beta}_i, \tag{34b}$$

where the first line of Eq. (34a) is the RRR of Ω_i obtained in Step 1, the least two lines are the RRR obtained in Step 2 for the adjacent internal cells. B_i is a system of $2+5\times 2=12$ equations ($2+5=7$ equations for case with only one neighboring internal cell). Therefore, they are sufficient to obtain the RRR of Step 2. The same procedure can be applied in Step 3. Although the above mentioned procedure can obtain the same degree reconstruction polynomials on the boundary cells as on the boundary cells, sometimes numerical instability will occur. It is found that when one order lower reconstruction polynomials are adopted on the boundary cells, the computation can be stable. Therefore, in the present paper, the accuracy of the boundary cells is one order lower than that of the internal cells. The physical boundary conditions are applied directly in the numerical fluxes.

3.3 High Order Multi-Step Finite Volume Scheme

Governing Equation

In this section, 2D Euler equations are presented as the governing equations that is

$$\frac{\partial \mathbf{U}}{\partial t}+\frac{\partial \mathbf{F}}{\partial x}+\frac{\partial \mathbf{G}}{\partial y}=0. \tag{35}$$

The conservative variables $\boldsymbol{U}$ and the inviscid flux $\boldsymbol{F},\boldsymbol{G}$ are given by

$$\mathbf{U}=\begin{bmatrix}\rho\\ \rho u\\ \rho v\\ \rho E\end{bmatrix},\quad \mathbf{F}=\begin{bmatrix}\rho u\\ \rho u^2+p\\ \rho uv\\ \rho uH\end{bmatrix},\quad \mathbf{G}=\begin{bmatrix}\rho v\\ \rho uv\\ \rho v^2+p\\ \rho vH\end{bmatrix}. \tag{36}$$

In Equation (36) ρ represents the density, p represents the pressure, u and v represent the x- and y- velocity component respectively, E and H represent the specific total energy and the specific total enthalpy respectively, where $E=\frac{1}{\gamma-1}\frac{p}{\rho}+\frac{1}{2}\left(u^2+v^2\right)$, $H=E+\frac{p}{\rho}$.

In finite volume method, we first integrate Equation (35) on the control volume e.g. element Ω_i

$$\frac{\partial}{\partial t}\int_{\Omega_i}\boldsymbol{U}d\Omega+\int_{\Omega_i}\nabla\cdot\Phi d\Omega=0, \tag{37}$$

where $\Phi=\left[\boldsymbol{F},\boldsymbol{G}\right]$. The application of Gauss theorem to Equation (37) yields

$$\frac{\partial}{\partial t}\int_{\Omega_i}\boldsymbol{U}d\Omega+\sum_{m=1}^{3}\int_{I_m}\Phi\cdot\boldsymbol{n}dl=0.$$

The introduction of the cell average of $\boldsymbol{U}$ defined similar to Eq.(23) leads to

$$\frac{\partial\bar{\boldsymbol{U}}_i}{\partial t}+\frac{1}{\left|\Omega_i\right|}\sum_{m=1}^{3}\int_{I_m}\Phi\cdot\boldsymbol{n}dl=0.$$

For high order FVS, integral on each side can be approximated with Gaussian quadrature:

$$\frac{\partial\bar{\boldsymbol{U}}_i}{\partial t}+\frac{1}{\left|\Omega_i\right|}\sum_{m=1}^{3}\left(l_m\sum_{ng=1}^{NG_m}w_{ng}\Phi\left(\boldsymbol{U}_{ng}\right)\cdot\boldsymbol{n}_m\right)=0, \tag{38}$$

where NG is the number of Gaussian points and $NG_m=2$ for a 4th-order FV schemes.

Curved boundary

The accuracy of high order schemes degrades with the general straight segments approximation of curved boundaries used in second order schemes [4]. The method of [45] is implemented to treat curved boundaries in this paper.

Limiter

The discontinuities of the solution lead to non-physical oscillations in the reconstruction procedure. In this paper, the WBAP-L2 limiter [46, 47] based on the secondary reconstruction [48] is used for capturing the discontinuities, which is

$$W = W^{L2}\left(1,\theta_1,\dots,\theta_J\right) = \frac{n_P + \sum_{k-1}^{J} 1/\theta_k^{p-1}}{n_P + \sum_{k-1}^{J} 1/\theta_k^{p}},$$

where parameters are set as $p = 4, n_P = 10$. To improve the efficiency, a problem-independent shock detector [48] is used to determine the "trouble cells" where the WBAP limiter is used. The smoothness indicator IS_i is defined as

$$IS_i = \frac{\sum_{j\in S_i}\left|u_i\left(\boldsymbol{x}_i\right) - u_j\left(\boldsymbol{x}_i\right)\right|}{N_i h_i^{(k+1)/2}\max\left(\bar{u}_j,\bar{u}_i\right)},$$

where N_i is the number of face-neighbor cells thus $N_i = 3$ for triangular cells. The shock detector is based on the utilization of the smoothness indicator:

$$\left(IS_i < \bar{S}_{dis}\right) = \begin{cases} True & \text{smooth region} \\ False & \text{shock region} \end{cases}.$$

In this paper, $\bar{S}_{dis}$ is chosen to be 1 for multi-step scheme and this parameter works well for numerical tests presented.

Numerical Flux

The reconstruction procedure provides the cellwise approximation of $\boldsymbol{U}$ to the flux function $\Phi\left(\boldsymbol{U}_{ng}\right)$ in Eq. (38). The flux can be evaluated with the flux splitting procedures, i.e.

$$\Phi\left(\boldsymbol{U}_{ng}\right)\cdot\boldsymbol{n}_m = \hat{\Phi}\left(\boldsymbol{U}^L\left(\boldsymbol{x}_{ng}\right),\boldsymbol{U}^R\left(\boldsymbol{x}_{ng}\right),\boldsymbol{n}_m\right).$$

The standard Riemann solver [49] is used in this paper with the entropy fix of Harten [50].

Temporal Discretization

The calculation of numerical fluxes leads Eq. (38) to an ODE of the time variable *t*. In this paper, a three stage TVD Runge-Kutta scheme [51] is implemented as we do in 1-D situation.

4 Numerical Results

Numerical tests are presented in this chapter. These tests demonstrate the property of multi-step scheme on 1-D and 2-D unstructured grids. 1-D tests are presented in Section 4.1; 2-D tests are presented in Section 4.2-4.4.

4.1 Shu-Osher problem

This test is another well-known problem which describes the interaction of an entropy sine wave with a Mach 3 right moving shock. The initial conditions are

$$\left(\rho_0,u_0,p_0\right) = \begin{cases} \left(3.857143, 2.629369, 10.33333\right) & \text{for } 0 \le x \le 0.5 \\ \left(1+0.2\sin\left(5x\right),0,1\right) & \text{otherwise} \end{cases} \quad \left(0 \le x \le 10\right)$$

In this test, 4th-order multi-step schemes with WBAP limiter are implemented. The computation domain contains 500 cells and the results are presented until $t = 1.8$. The density distribution of results is shown in Fig. 4. Numerical solution of the 5th order WENO scheme [30] using 20000 cells is used as the exact solution. These results also demonstrate high resolution of the scheme.

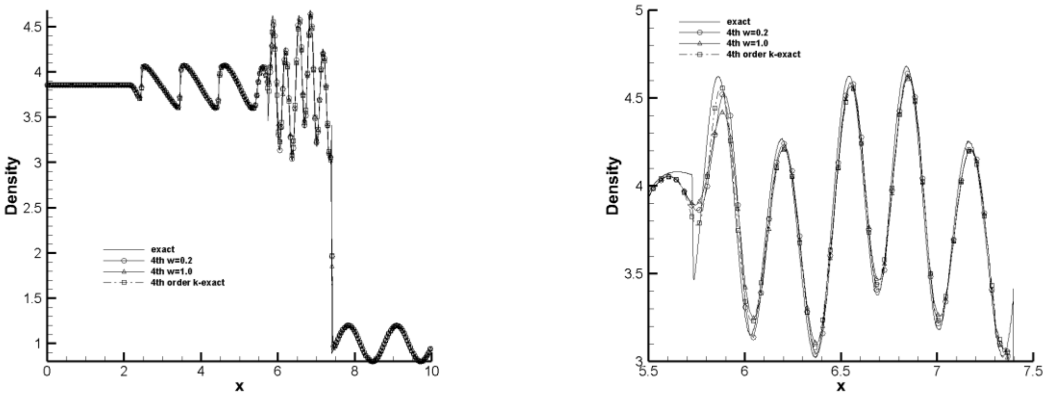

(a) Entire view (b) Enlargements

Fig. 4: Shu-Osher Problem. Density distribution at t=1.8.

4.2 Isentropic Vortex Problem

This test is chosen to assess the accuracy of multi-step scheme for evolution of a 2-D inviscid isentropic vortex in a free stream. The mean flow density, ρ_∞, velocity, u_∞ and v_∞, and pressure, p_∞ are considered to be a free stream. In this test, mean flow is $(\rho_\infty, u_\infty, v_\infty, p_\infty) = (1,1,1,1)$ and the computational domain is $[0,10]\times[0,10]$ with periodic boundaries in two directions.

An isentropic vortex is added to the mean flow field as an initial condition. The following perturbation values are given by

$$
\begin{aligned}
(\delta u, \delta v) &= \frac{\chi}{2\pi} e^{0.5(1-r^2)}(-\bar{y}, \bar{x}), \\
\delta T &= -\frac{(\gamma-1)\chi^2}{8\gamma\pi^2} e^{1-r^2}, \\
\delta\left(S = p/\rho^r\right) &= 0,
\end{aligned}
$$

where $(\bar{x}, \bar{y}) = (x-5, y-5)$, $r^2 = \bar{x}^2 + \bar{y}^2$, $\gamma = 1.4$ and χ is the vortex strength. Here $\chi = 5$ and $T = \frac{p}{\rho}$. The results are presented until $t = 2.0$. There are 2 types of grids used in the numerical computation, namely regular and irregular grids as Fig. 5.

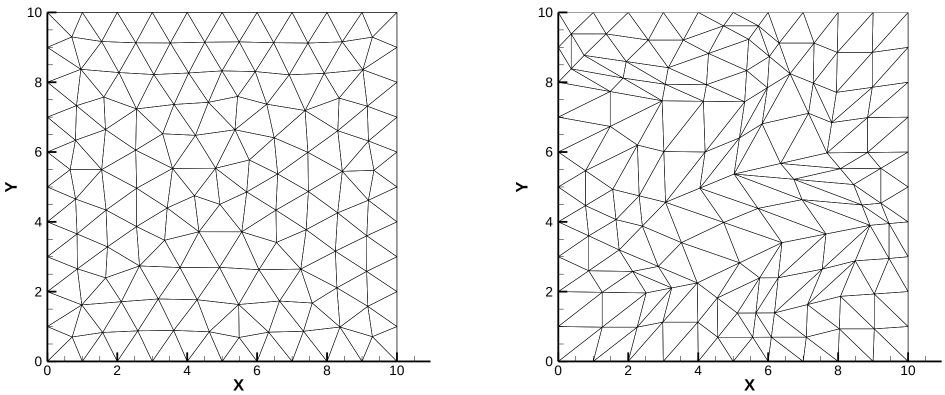

Fig. 5: Regular and irregular grids for the isentropic vortex problem with size $h = 1$

The grid sizes are chosen to be 1 to $1/16$. The CFL number is chosen to be 1. The exact solution is a convection of the vortex with the mean flow and thus the accuracy can be easily calculated. In this test, accuracy of 3rd and 4th order multi-step schemes on regular grids are presented in Table 1 compared with corresponding order k-exact schemes. Tests on irregular grids are presented in Table 2. The weight ω in multi-step schemes are chosen to be 1 and 0.5.

Table 1: Accuracy tests for the isentropic vortex problem on regular grids

Schemes	Grid Size	L_1 error	Order	L_∞ error	Order
4th order Multi-Step w=1.0	1	3.69E-03		4.41E-02	
	1/2	4.87E-04	2.92	1.09E-02	2.02
	1/4	2.73E-05	4.16	5.97E-04	4.19
	1/8	1.22E-06	4.48	3.08E-05	4.28
	1/16	7.23E-08	4.08	1.69E-06	4.19
4th order Multi-Step w=0.5	1	3.72E-03		4.34E-02	
	1/2	4.56E-04	3.03	1.08E-02	2.01
	1/4	2.57E-05	4.15	5.99E-04	4.17
	1/8	1.12E-06	4.52	2.91E-05	4.36
	1/16	6.18E-08	4.18	1.71E-06	4.08
4th order k-exact	1	4.41E-03		4.63E-02	
	1/2	4.21E-04	3.39	1.05E-02	2.14
	1/4	2.66E-05	3.98	5.31E-04	4.31
	1/8	1.21E-06	4.45	3.24E-05	4.04
	1/16	7.12E-08	4.09	1.69E-06	4.26
3rd order Multi-Step w=1.0	1	8.17E-03		1.22E-01	
	1/2	1.71E-03	2.26	3.13E-02	1.96
	1/4	2.89E-04	2.57	5.57E-03	2.49
	1/8	3.84E-05	2.91	7.67E-04	2.86
	1/16	4.77E-06	3.01	1.02E-04	2.91
3rd order Multi-Step w=0.5	1	7.35E-03		9.98E-02	
	1/2	1.43E-03	2.36	2.70E-02	1.89
	1/4	2.36E-04	2.61	4.67E-03	2.53
	1/8	3.08E-05	2.94	6.25E-04	2.90
	1/16	3.80E-06	3.02	8.48E-05	2.88

Table 2: Accuracy tests for the isentropic vortex problem on irregular grids

Schemes	Grid Size	L_1 error	Order	L_∞ error	Order
4th order Multi-Step w=1.0	1	1.01E-02		1.68E-01	
	1/2	2.29E-03	2.14	4.57E-02	1.88
	1/4	2.71E-04	3.08	6.12E-03	2.90
	1/8	2.06E-05	3.72	5.02E-04	3.61
	1/16	1.39E-06	3.89	3.31E-05	3.92
4th order Multi-Step w=0.5	1	1.01E-02		1.67E-01	
	1/2	2.26E-03	2.16	4.40E-02	1.92
	1/4	2.67E-04	3.08	6.06E-03	2.86
	1/8	1.81E-05	3.88	4.42E-04	3.78

	1/16	1.12E-06	4.02	2.66E-05	4.05
4th order k-exact	1	1.03E-02		1.59E-01	
	1/2	2.07E-03	2.31	3.74E-02	2.08
	1/4	2.16E-04	3.26	3.51E-03	3.41
	1/8	1.19E-05	4.18	2.35E-04	3.90
	1/16	5.59E-07	4.41	1.16E-05	4.34
3rd order Multi-Step w=1.0	1	1.27E-02		1.91E-01	
	1/2	4.99E-03	1.35	8.43E-02	1.18
	1/4	1.18E-03	2.08	2.28E-02	1.89
	1/8	2.02E-04	2.55	3.86E-03	2.56
	1/16	2.78E-05	2.86	5.50E-04	2.81
3rd order Multi-Step w=0.5	1	1.30E-02		1.92E-01	
	1/2	4.72E-03	1.46	7.83E-02	1.29
	1/4	1.09E-03	2.12	2.10E-02	1.90
	1/8	1.81E-04	2.59	3.45E-03	2.60
	1/16	2.46E-05	2.88	4.79E-04	2.85

In Table 1 and 2, the numerical accuracy of multi-step scheme is demonstrated to reach the accuracy as supposed to be in Section 3. The error can be reduced by the choice of weight. The results show that the accuracy of multi-step scheme is very close to the accuracy of k-exact scheme. The accuracy and the efficiency comparison are shown in Fig. 6 and Fig. 7, respectively. In Fig. 7, the efficiency of multi-step scheme also approximates the efficiency of k-exact scheme, which indicates that the excursive steps do not cost too much computational resource.

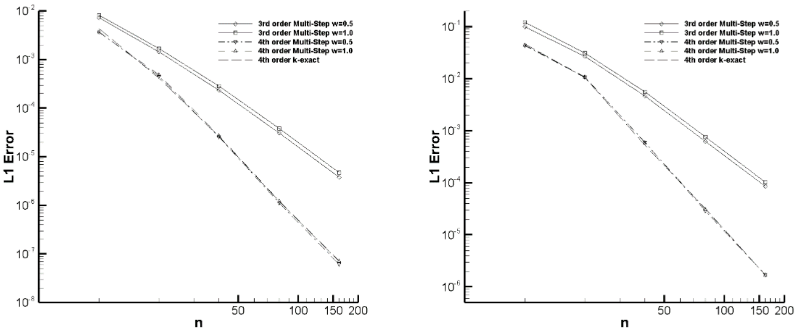

Fig. 6: Accuracy comparison for the isentropic vortex problem on regular grids

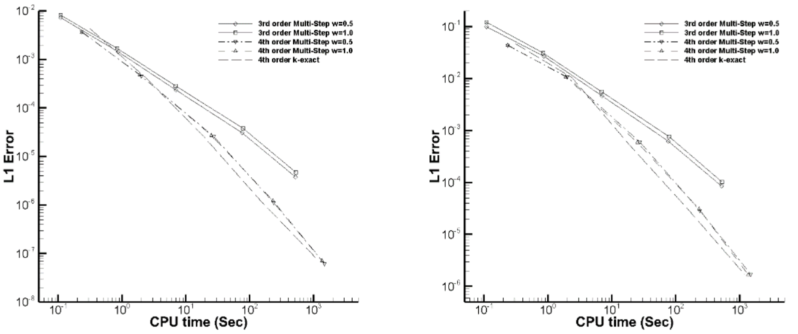

Fig. 7: Efficiency comparison for the isentropic vortex problem on regular grids

4.3 Subsonic Flows past a Circular Cylinder

This test is chosen to assess the accuracy of multi-step scheme with boundary treatments for the subsonic flow past a circular cylinder at a Mach number of $M_\infty = 0.38$ [52]. The problem is calculated with curved boundaries. The five successively refined O-type grids used in this test are shown in Fig. 8, which consist of 16×9, 32×17, 64×33, 128×65 and 256×129 grid points, respectively. The first number refers to the number of points in the circular direction, and the second refers to the number of concentric circles in the mesh. The radius of the cylinder is $r_1 = 0.5$, the domain is bounded by $r_{129} = 40$, and the radii of concentric circles for 256×129 mesh are set up as

$$r_i = r_1\left(1+\frac{2\pi}{256}\sum_{j=1}^{i-1}\alpha^j\right),\ i = 2,\ldots,129,$$

where $\alpha = 1.03803945$. The coarser grids are generated by successively un-refining the finest mesh.

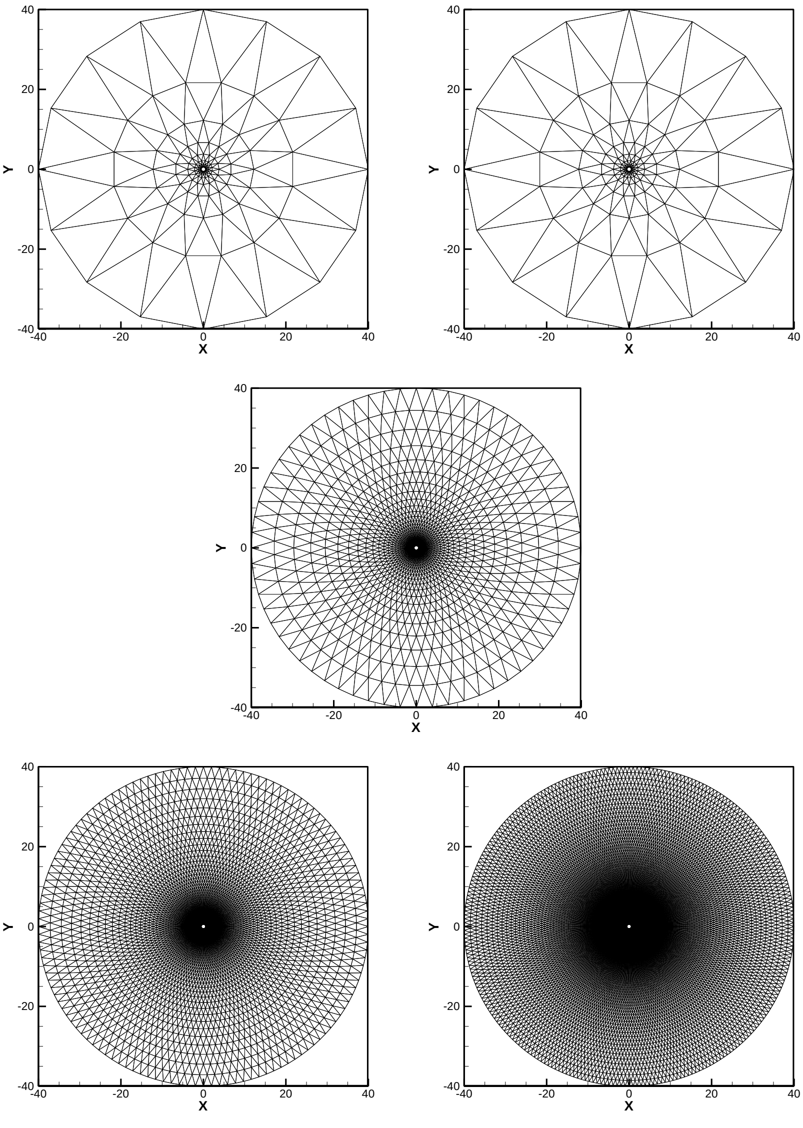

Fig. 8: Sequences of five successively globally refined meshes for the subsonic flow past a circular cylinder problem

The CFL number used in temporal discretization is 1. In this test, To measure the order of accuracy, we used the following entropy production ε that

$$\varepsilon \doteq \frac{p}{p_\infty}\left(\frac{\rho_\infty}{\rho}\right)^{\gamma} - 1 \tag{39}$$

as the error measurement. The errors on norm L_1 and L_2 are presented in Table 3 and the results demonstrate that the expected order of accuracy can be achieved.

Table 3 Accuracy tests for the subsonic flow past a circular cylinder problem

Schemes	Grid Size	L1 error	Order	L2 error	Order
4th order Multi-Step w=1.0	16×9	1.61E-02		3.78E-02	
	32×17	1.69E-03	3.25	6.34E-03	2.58
	64×33	1.08E-04	3.97	6.10E-04	3.38
	128×65	6.84E-06	3.98	5.42E-05	3.49
	256×129	4.64E-07	3.88	4.87E-06	3.48
4th order Multi-Step w=0.5	16×9	1.40E-02		3.16E-02	
	32×17	1.29E-03	3.44	4.88E-03	2.69
	64×33	8.43E-05	3.94	4.74E-04	3.37
	128×65	5.97E-06	3.82	4.34E-05	3.45
	256×129	4.74E-07	3.66	6.88E-06	2.66
3rd order Multi-Step w=1.0	16×9	1.30E-02		3.05E-02	
	32×17	2.44E-03	2.41	7.52E-03	2.02
	64×33	3.15E-04	2.95	1.16E-03	2.69
	128×65	3.89E-05	3.02	1.74E-04	2.74
	256×129	4.86E-06	3.00	2.75E-05	2.66
3rd order Multi-Step w=0.5	16×9	1.10E-02		2.52E-02	
	32×17	2.06E-03	2.42	6.10E-03	2.05
	64×33	2.91E-04	2.82	1.02E-03	2.57
	128×65	3.89E-05	2.90	1.70E-04	2.59
	256×129	5.13E-06	2.92	2.90E-05	2.55

4.4 Double Mach Reflection of a strong shock wave

This test [53] is a well-known case for high resolution scheme. The computational domain is $[0,4]\times[0,1]$. An incident shock $Ma=10$ is located at $(1/6,0)$, inclined 60° with respect to the x-axis. The results are presented until $t=0.2$.

The mesh size in this test is $1/240$ and the CFL number is 1. The WBAP limiter which is presented in Section 3 is used in computations. In this test, numerical solutions of 3rd- and 4th-order schemes are presented with the density contours shown in Fig. 9 and 10. In Fig. 9 and 10, it is clear that all solutions oscillation-free and higher order schemes can capture the complicated flow structures near the Mach stem better that lower ones. Comparing to the k-exact schemes, multi-step schemes demonstrate the higher resolution of the shear layer and the vortex.

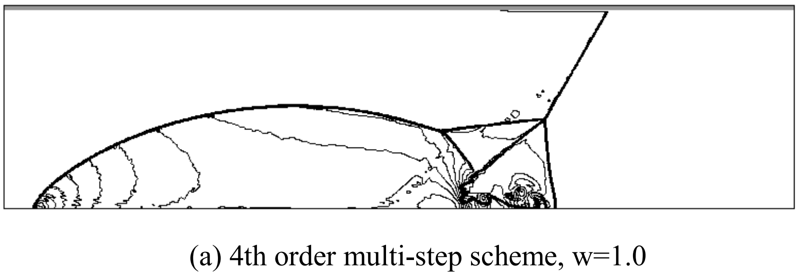

(a) 4th order multi-step scheme, w=1.0

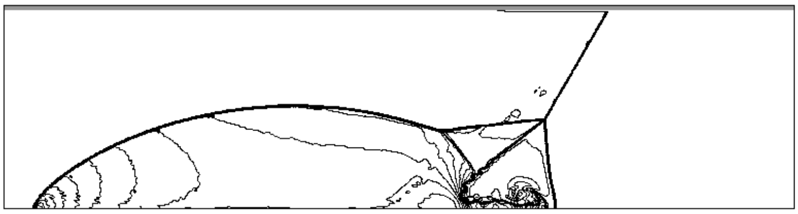

(b) 4th order multi-step scheme, w=0.5

Fig. 9: Comparison of density contours for double Mach reflection on grids with size h = 1/240. Thirty equally spaced contour lines between 2.05 and 21.31.

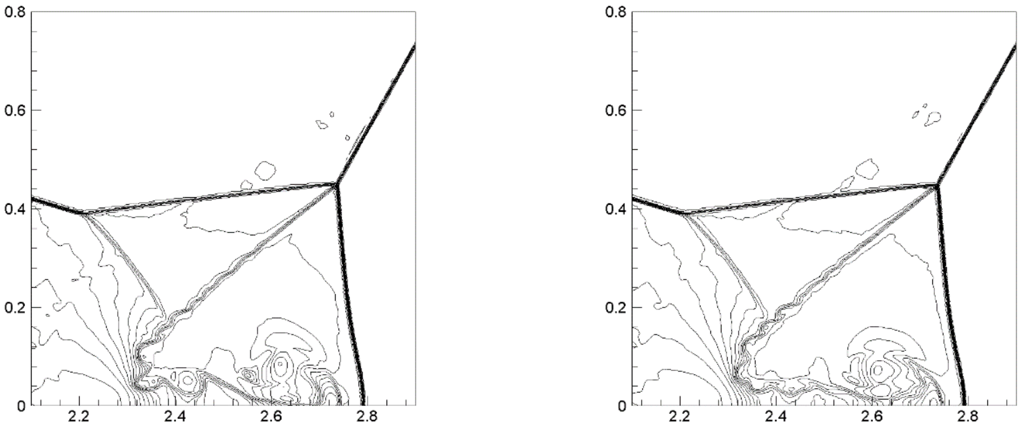

(a) 4th order multi-step scheme, w=1.0 (b) 4th order multi-step scheme, w=0.5

Fig. 10: Close-up view around the double Mach stem of Fig. 9.

5 Conclusion

In this paper, MSR procedure is presented for finite volume method on both 1D grids and 2D unstructured grids. The procedure consists of several recursive steps and in each step, the RRR on the face-neighboring cells after applying the CT and those on the current cell are utilized to solve coefficients of higher order polynomials. In 1D case, the Fourier analysis is presented to study the dispersion/dissipation properties of the semi-discretized FV schemes based on the MSR for solving the scalar linear advection equation. In 2D case, the application of the MSR in high order FV schemes solving 2D Euler equations are presented in detail. Several numerical tests are solved to show the properties of multi-step schemes. The advantage of the present schemes is that they can achieve arbitrarily high order of accuracy on compact stencil.

Acknowledgements

This work is supported by the National Natural Science Foundation of China (Grant No. 91752114 and 11672160). The 2D finite volume method framework is based on Qian Wang's code.

Appendix A

In this appendix, the CT for the 1D and 2D cases are presented in detail. To ensure that the CT preserving the k-exactness of the reconstruction, the CT is derived assuming the exact solution is a cubic polynomial.

1D case

We assume that $u(x)$ is in the form of

$$u_i(x) = u_i + u_i'(x - x_i) + \frac{1}{2!}u_i''(x - x_i)^2 + \frac{1}{3!}u_i'''(x - x_i)^3 \tag{A.1}$$

where subscript *i* denotes value at point x_i. In MSR, *u* is approximated as

$$u_i(x) = \bar{u}_i + \sum_{l=1}^{3} u_i^l \phi_{l,i}(x) \tag{A.2}$$

Comparing Equation (A.1) and Equation (A.2), the relationship between derivatives $u_i^{(l)}$ and coefficients u_i^l can be derived as

$$\begin{bmatrix} u_i^{(1)} \\ u_i^{(2)} \\ u_i^{(3)} \end{bmatrix} = \begin{bmatrix} 1/h_i & 0 & 0 \\ 0 & 2!/h_i^2 & 0 \\ 0 & 0 & 3!/h_i^3 \end{bmatrix} \begin{bmatrix} u_i^1 \\ u_i^2 \\ u_i^3 \end{bmatrix}$$

which can be denoted as

$$\boldsymbol{u}_i^D = R_i \boldsymbol{u}_i \tag{A.3}$$

Equation (A.3) is then substituted into Equation (A.1)

$$u_i(x) = u_i + u_i^1(\delta x_i) + u_i^2(\delta x_i)^2 + u_i^3(\delta x_i)^3 \tag{A.4}$$

When the relationship (A.3) holds, the equivalence between Equation (A.1) and (A.2) requires the equivalence of constant term of two equations

$$u_i = \bar{u}_i - \sum_{i=1}^{3} \frac{u_i^l}{h_i} \int_{\Omega_i} \overline{(\delta x_i)^l} dx \tag{A.5a}$$

or the equivalent form

$$\bar{u}_i = u_i + \sum_{i=1}^{3} \frac{u_i^l}{h_i} \int_{\Omega_i} \overline{(\delta x_i)^l} dx \tag{A.5b}$$

Equation (A.5b) can be derived straightforward by integrating (A.4) in cell Ω_i. This means Equation (A.3) is exact. Taylor expansions of derivate $u_j^{(l)}$ at x_i gives

$$\begin{cases} u_j^{(1)} = u_i^{(1)} + u_i^{(2)}(x_j - x_i) + \frac{1}{2!}u_i^{(3)}(x)(x_j - x_i)^2 \\ u_j^{(2)} = u_i^{(2)} + u_i^{(3)}(x_j - x_i) \\ u_j^{(3)} = u_i^{(3)} \end{cases}$$

The expansion terms are up to 3rd derivative terms since *u* follows cubic polynomial distribution. These expansions lead to transformation from $\boldsymbol{u}_i^D$ to $\boldsymbol{u}_j^D$

$$\boldsymbol{u}_j^D = \begin{bmatrix} 1 & x_j - x_i & (x_j - x_i)/2 \\ 0 & 1 & x_j - x_i \\ 0 & 0 & 1 \end{bmatrix} \boldsymbol{u}_i^D$$

which can be denoted as

$$\boldsymbol{u}_j^D = \tilde{T}_{j \to i} \boldsymbol{u}_i^D \tag{A.6}$$

Introduction of Equation (A.3) into (A.6) yields

$$\boldsymbol{u}_j = R_j^{-1} \boldsymbol{u}_j^D = R_j^{-1} \tilde{T}_{j \to i} \boldsymbol{u}_i^D = R_j^{-1} \tilde{T}_{j \to i} R_i \boldsymbol{u}_i$$

Then the CT is given by

$$\boldsymbol{u}_j = T_{j(\to i)} \boldsymbol{u}_i$$

with

$$T_{j\to i} = R_j^{-1}\tilde{T}_{j\to i}R_i \,.$$

2D case

The CT of the 2D case can be derived similarly as the 1D case. The resulting transformation matrix is a a 9×9 square matrix given by

$$T_{j\to i} = R_j^{-1}\tilde{T}_{j\to i}R_i$$

The forms of $\tilde{T}_{j\to i}$ and R_i are

$$\tilde{T}_{j\to i} = \begin{bmatrix}
1 & 0 & \Delta x_{ji} & \Delta y_{ji} & 0 & \frac{1}{2!}\Delta x_{ji}^2 & \Delta x_{ji}\Delta y_{ji} & \frac{1}{2!}\Delta y_{ji}^2 & 0 \\
0 & 1 & 0 & \Delta x_{ji} & \Delta y_{ji} & 0 & \frac{1}{2!}\Delta x_{ji}^2 & \Delta x_{ji}\Delta y_{ji} & \frac{1}{2!}\Delta y_{ji}^2 \\
0 & 0 & 1 & 0 & 0 & \Delta x_{ji} & \Delta y_{ji} & 0 & 0 \\
0 & 0 & 0 & 1 & 0 & 0 & \Delta x_{ji} & \Delta y_{ji} & 0 \\
0 & 0 & 0 & 0 & 1 & 0 & 0 & \Delta x_{ji} & \Delta y_{ji} \\
0 & 0 & 0 & 0 & 0 & 1 & 0 & 0 & 0 \\
0 & 0 & 0 & 0 & 0 & 0 & 1 & 0 & 0 \\
0 & 0 & 0 & 0 & 0 & 0 & 0 & 1 & 0 \\
0 & 0 & 0 & 0 & 0 & 0 & 0 & 0 & 1
\end{bmatrix}$$

and

$$R_i = diag\left(h_i^{-1}, h_i^{-1}, 2!h_i^{-2}, h_i^{-2}, 2!h_i^{-2}, 3!h_i^{-3}, 2!h_i^{-3}, 2!h_i^{-3}, 3!h_i^{-3}\right),$$

respectively, where $\Delta x_{ji} = x_j - x_i$, $\Delta y_{ji} = y_j - y_i$ and length scale is given by

$$h_i = \max\left(r_i, \sqrt{|\Omega_i|}\right).$$

Reference

[1] Z.J. Wang, Y. Liu, G. May, A. Jameson, Spectral difference method for unstructured grids II: extension to the Euler equations, J. Sci. Comput. 32(1) (2007) 45-71.

[2] T.J. Barth, P.O. Frederickson, Higher order solution of the Euler equations on unstructured grids using quadratic reconstruction, AIAA Pap. 90 (1990) 0013.

[3] M. Delanaye, Y. Liu, Quadratic reconstruction finite volume schemes on 3D arbitrary unstructured polyhedral grids, AIAA Pap. 9(9) (1989) 3259.

[4] C. Ollivier-Gooch, M. Van Altena, A high-order-accurate unstructured mesh finite-volume scheme for the advection-diffusion equation, J. Comput. Phys. 181(2) (2002) 729-752.

[5] C.F. Ollivier-Gooch, Quasi-ENO schemes for unstructured meshes based on unlimited data-dependent least-squares reconstruction, J. Comput. Phys. 133(1) (1997) 6-17.

[6] Friedrich, Weighted essentially non-oscillatory schemes for the interpolation of mean values on unstructured grids, J. Comput. Phys. 144(1) (1998) 194-212.

[7] M. Dumbser, M. Käser, Arbitrary high order non-oscillatory finite volume schemes on unstructured meshes for linear hyperbolic systems, J. Comput. Phys. 221(2) (2007) 693-723.

[8] M. Dumbser, M. Käser, V.A. Titarev, E.F. Toro, Quadrature-free non-oscillatory finite volume schemes on unstructured meshes for nonlinear hyperbolic systems, J. Comput. Phys. 226(1) (2007) 204-243.

[9] C. Hu, C.W. Shu, Weighted essentially non-oscillatory schemes on triangular meshes, J. Comput. Phys. 150(1) (1999) 97-127.

[10] W.H. Reed, T.R. Hill, Triangular mesh methods for the neutron transport equation, Los Alamos report LA-UR-73-479, 1973.

[11]B. Cockburn, C.W. Shu, TVB Runge-Kutta local projection discontinuous Galerkin finite element method for conservation laws. II. General framework, Math. Comput. 52(186) (1989) 411-435.
[12]B. Cockburn, S.Y. Lin, C.W. Shu, TVB Runge-Kutta local projection discontinuous Galerkin finite element method for conservation laws III: one-dimensional systems, J. Comput. Phys. 84(1) (1989) 90-113.
[13]B. Cockburn, S. Hou, C.W. Shu, The Runge-Kutta local projection discontinuous Galerkin finite element method for conservation laws. IV. The multidimensional case, Math. Comput. 54(190) (1990) 545-581.
[14]B. Cockburn, C.W. Shu, Runge-Kutta discontinuous Galerkin methods for convection-dominated problems, J. Sci. Comput. 16(3) (2001) 173-261.
[15]Z.J. Wang, Spectral (finite) volume method for conservation laws on unstructured grids: basic formulation, J. Comput. Phys. 178(1) (2002) 210-251.
[16]Z.J. Wang, Y. Liu, Spectral (finite) volume method for conservation laws on unstructured grids: II. Extension to two-dimensional scalar equation, J.Comput. Phys. 179(2) (2002) 665-697.
[17]Z.J. Wang, Y. Liu, Spectral (finite) volume method for conservation laws on unstructured grids III: one dimensional systems and partition optimization, J. Sci. Comput. 20(1) (2004) 137-157.
[18]Z.J. Wang, L. Zhang, Y. Liu, Spectral (finite) volume method for conservation laws on unstructured grids IV: extension to two-dimensional systems, J.Comput. Phys. 194(2) (2004) 716-741.
[19]Y. Liu, M. Vinokur, Z.J. Wang, Spectral difference method for unstructured grids I: basic formulation, J. Comput. Phys. 216(2) (2006) 780-801.
[20]Z.J. Wang, Y. Liu, G. May, A. Jameson, Spectral difference method for unstructured grids II: extension to the Euler equations, J. Sci. Comput. 32(1) (2007) 45-71.
[21]G. May, A. Jameson, A spectral difference method for the Euler and Navier-Stokes equations on unstructured meshes, AIAA Pap. 304 (2006).
[22]M. Dumbser, D.S. Balsara, E.F. Toro, C.D. Munz, A unified framework for the construction of one-step finite volume and discontinuous Galerkin schemes on unstructured meshes, J. Comput. Phys. 227(18) (2008) 8209-8253.
[23]M. Dumbser, Arbitrary high order PNPMschemes on unstructured meshes for the compressible Navier-Stokes equations, Comput. Fluids 39(1) (2010) 60-76.
[24]M. Dumbser, O. Zanotti, Very high order PNPMschemes on unstructured meshes for the resistive relativistic MHD equations, J. Comput. Phys. 228(18) (2009) 6991-7006.
[25]Zhang, L., Liu, W., He, L., Deng, X., & Zhang, H., A class of hybrid DG/FV methods for conservation laws I: Basic formulation and one-dimensional systems, J. Comput. Phys. 231(4) (2012) 1081-1103.
[26]Zhang, L., Liu, W., He, L., Deng, X., & Zhang, H., A class of hybrid DG/FV methods for conservation laws II: Two-dimensional cases, J. Comput. Phys. 231(4) (2012) 1104-1120.
[27]A. Harten, B. Engquist, S. Osher, S.R. Chakravarthy, Uniformly high order accurate essentially non-oscillatory schemes III, J. Comput. Phys. 71(2) (1987) 231-303.
[28]C.W. Shu, S. Osher, Efficient implementation of essentially non-oscillatory shock-capturing schemes, J. Comput. Phys. 77(2) (1988) 439-471.
[29]C.W. Shu, S. Osher, Efficient implementation of essentially non-oscillatory shock-capturing schemes, II, J. Comput. Phys. 83(1) (1989) 32-78.
[30]G.S. Jiang, C.W. Shu, Efficient implementation of weighted ENO schemes, J. Comput. Phys. 126(1) (1996) 202-228.
[31]D.S. Balsara, C.W. Shu, Monotonicity preserving weighted essentially non-oscillatory schemes with increasingly high order of accuracy, J. Comput. Phys. 160(2) (2000) 405-452.
[32]A.K. Henrick, T.D. Aslam, J.M. Powers, Simulations of pulsating one-dimensional detonations with true fifth order accuracy, J. Comput. Phys. 213(1) (2006) 311-329.
[33]R. Borges, M. Carmona, B. Costa, W.S. Don, An improved weighted essentially non-oscillatory scheme for hyperbolic conservation laws, J. Comput. Phys. 227(6) (2008) 3191-3211.
[34]D.S. Balsara, T. Rumpf, M. Dumbser, C.D. Munz, Efficient, high accuracy ADER-WENO schemes for hydrodynamics and divergence-free magnetohydro-dynamics, J. Comput. Phys. 228(7) (2009) 2480-2516.
[35]D.S. Balsara, Divergence-free reconstruction of magnetic fields and WENO schemes for

magnetohydrodynamics, J. Comput. Phys. 228(14) (2009) 5040-5056.
[36]R. Abgrall, On essentially non-oscillatory schemes on unstructured meshes: analysis and implementation, J. Comput. Phys. 114(1) (1994) 45-58.
[37]R. Abgrall, A. Larat, M. Ricchiuto, Construction of very high order residual distribution schemes for steady inviscid flow problems on hybrid unstructured meshes, J. Comput. Phys. 230(11) (2011) 4103-4136.
[38]Q. Wang, Y.X. Ren, W. Li, Compact high order finite volume method on unstructured grids I: Basic formulations and one-dimensional schemes, J. Comput. Phys., 314 (2016) 863-882.
[39]Q. Wang, Y.X. Ren, W. Li, Compact high order finite volume method on unstructured grids II: Extension to two-dimensional Euler equations, J. Comput. Phys., 314 (2016) 883-904.
[40]Q. Wang, Y.X. Ren, W. Li, Compact high order finite volume method on unstructured grids III: Variational reconstruction, J. Comput. Phys., 337 (2017) 1-26.
[41]H.Q. Yang, Z.J. Chen, A. Przekwas, J. Dudley, A high-order CFD method using successive differentiation, J. Comput. Phys., 281 (2015) 690-707.
[42]Florian Haider, Bernard Courbet, Jean-Pierre Croisille. A high-order compact reconstruction for finite volume methods: the one-dimensional case. 2015. <hal-01284635>
[43]M.P. Martín, E.M. Taylor, M. Wu, V.G. Weirs, A bandwidth-optimized WENO scheme for the effective direct numerical simulation of compressible turbulence, J. Comput. Phys. 220(1) (2006) 270-289.
[44]S.K. Lele, Compact finite difference schemes with spectral-like resolution, J. Comput. Phys. 103(1) (1992) 16-42.
[45]W. Li, Y.X. Ren, The multi-dimensional limiters for discontinuous Galerkin method on unstructured grids, Comput. Fluids 96 (2014) 368-376.
[46]W. Li, Y.X. Ren, The multi-dimensional limiters for solving hyperbolic conservation laws on unstructured grids II: extension to high order finite volume schemes, J. Comput. Phys. 231(11) (2012) 4053-4077.
[47]W. Li, Y.X. Ren, G. Lei, H. Luo, The multi-dimensional limiters for solving hyperbolic conservation laws on unstructured grids, J. Comput. Phys. 230(21) (2011) 7775-7795.
[48]W. Li, Y.X. Ren, High-order k-exact WENO finite volume schemes for solving gas dynamic Euler equations on unstructured grids, Int. J. Numer. Methods Fluids 70(6) (2012) 742-763.
[49]Roe, P. L., Approximate Riemann solvers, parameter vectors, and difference schemes. J. Comput. Phys., 43(2) (1981) 357-372.
[50]A. Harten and J. M. Hyman. Self Adjusting Grid Methods for One-Dimensional Hyperbolic Conservation Laws. J. Comput. Phys., 50 (1983) 235-269.
[51]C.W. Shu, S. Osher, Efficient implementation of essentially non-oscillatory shock-capturing schemes, J. Comput. Phys. 77(2) (1988) 439-471.
[52]Luo, H., Baum, J. D., & Löhner, R., A Hermite WENO-based limiter for discontinuous Galerkin method on unstructured grids, J. of Comput. Phys., 225(1) (2007) 686-713.
[53]Woodward, P., & Colella, P., The numerical simulation of two-dimensional fluid flow with strong shocks, J. of Comput. Phys., 54(1) (1984) 115-173.